1994ApJ...426..116K

THE ASTROPHYSICAL JOURNAL, 426:116–122, 1994 May 1

ISOLATING THE PHYSICAL PARAMETERS OF SYNCHROTRON SOURCES

DEBORA M. KATZ-STONE AND LAWRENCE RUDNICK
Astronomy Department, University of Minnesota, 116 Church Street SE, Minneapolis, MN 55455
Received 1993 July 15; accepted 1993 November 4

ABSTRACT

We introduce a technique to correct synchrotron brightness maps for their dependence on observing frequency. This correction depends on the shape or "colors" of the synchrotron spectrum and corresponds to the *K*-correction used for photometry of redshifted galaxies.

Using this corrected map and a spectral index map, we are able to isolate the contributions of pairs of the three physical parameters: the number of relativistic electrons along the line of sight, N_T; the magnetic field strength, B; and a fiducial energy, γ_0, that characterizes the electron energy distribution. Thus by constructing maps of N_T/γ_0^2, $\gamma_0^2 B$, and $N_T B$ and looking for differences in the maps of these three quantities, we can, in principle, determine the parameter that dominates the emissivity for a given feature.

We have applied this technique to the Carilli et al. (1991) maps of the radio galaxy Cygnus A. The resulting color-corrected map of the eastern lobe is dominated by an edge-brightened channel which straddles the counterjet, is itself girdled by rings, and is seen at low contrast in the original maps. No counterpart to this channel has yet been seen in two-dimensional or three-dimensional jet simulations. Our analysis leads us to conclude that it is dominated by a density enhancement.

Subject headings: acceleration of particles — galaxies: individual (Cygnus A) — radiation mechanisms: nonthermal — radio continuum: galaxies

1. INTRODUCTION

The most basic challenge in understanding extended sources of sychrotron emission is the derivation of physical parameters from the observations. This is difficult because (1) source structures can be strongly influenced by the presence of an unseen thermal plasma; (2) the synchrotron emissivity depends on a combination of factors—the magnetic field and the relativistic particle energy and number—which have not proved possible to be separated; and (3) variations in the spectral index within a source means that the structures we see are observing frequency–dependent. Our maps typically cover a range of $\leq 10^{2.5}$ in frequency; how would the sources appear if we could observe them with high resolution and dynamic range from 10^6 to 10^{20} Hz?

Today's analyses of extragalactic synchrotron sources closely resemble the state of the art reviewed by Miley (1976). Miley summarized how observations of the total intensity and spectral index maps could be used, with a considerable number of assumptions, to derive such parameters as the minimum energy density and its corresponding magnetic field. Although there have been many important advances in the past two decades, such as hydrodynamical modeling (e.g., Norman et al. 1982; Bicknell 1986), the introduction of in situ particle acceleration (e.g., Meisenheimer et al. 1989), and the study of associated emission-line material (e.g., van Breugel et al. 1985), the basic problem of isolating the synchrotron emission factors still remains. In this paper, we introduce a method of producing frequency-independent maps, and isolating the relative contributions of these parameters, by adding knowledge of the shape of the relativistic electron energy distribution to the total intensity and spectral index maps utilized in the past. Although this new technique also rests on some assumptions about the electron population, it provides a powerful tool for the analysis of extragalactic sources.

In § 2, we illustrate the color-correction method to eliminate frequency dependence of the emissivity. In § 3, we demonstrate the process of isolating the various physical parameter pairs. In § 4, we apply this color correction to Cygnus A and discuss the resulting maps.

2. THE SYNCHROTRON COLOR-CORRECTION PROCEDURE

In this section, we will describe the construction of a new set of maps, which are independent of the observing frequency and which depend on the underlying physical parameters in different ways. We begin by describing a "correction" procedure to the monochromatic maps.

The correction procedure depends on the assumption that the broad-band spectral shape is known at each point in the source and that this shape is constant for at least some region or feature. In the case of Cygnus A, we found that we could fit the *synchrotron spectrum* at every position in the lobes with a *single* curve if we allowed the spectrum at each position to shift in both log (ν) and log (I) (Katz-Stone, Rudnick, & Anderson 1993, hereafter KRA). In this paper, we make the further reasonable assumption that if the shape of the *synchrotron spectrum* is invariant, then the shape of the *relativistic electron energy distribution* is invariant, and that all variations in brightness are due to changes in total relativistic particle density, or in magnetic field or by scalings of all particle energies.

2.1. *The Definition of a Frequency-independent Synchrotron Brightness Measure*

For a single relativistic electron in a magnetic field, B, the energy loss rate due to synchrotron emission is given by

$$\frac{dE}{dt} \propto \frac{d\gamma}{dt} \propto -(\gamma B)^2 ,$$

where

$$\gamma = \frac{E}{m_e c^2} .$$

Most of this energy is radiated around a critical frequency, $\nu_c \propto \gamma^2 B$. As long as the number of electrons is decreasing sufficiently rapidly with energy [e.g., $N(\gamma) \propto \gamma^{-1}$], then most of the radiation at an observed frequency, ν, will come from electrons of energy $\gamma \propto (\nu/B)^{1/2}$. This approximation simplifies the expressions below but does not affect the scaling relationships we derive.

For a population of electrons with an energy density distribution, $n(\gamma)$, the emissivity, ϵ, at frequency, ν, can be written as

$$\epsilon(\nu)d\nu \propto -\frac{d\gamma}{dt}\, n(\gamma)d\gamma$$

(see, for example, Longair 1981).

We rewrite $n(\gamma)$ in terms of a unitless variable, $f(\gamma/\gamma_0)$, such that

$$n(\gamma) = \frac{n_T}{\gamma_0} f\left(\frac{\gamma}{\gamma_0}\right) ,$$

where n_T is the total density of relativistic electrons within a certain volume, integrated over all energies, and γ_0 is a fiducial γ such that

$$\frac{1}{\gamma_0} \int_{\gamma_{\min}}^{\gamma_{\max}} f\left(\frac{\gamma}{\gamma_0}\right) d\gamma \equiv 1$$

for any value that γ_0 may have throughout the source. For the simplified case discussed in this paper, we will assume that since only scaling changes occur in γ, that $\gamma_{\max}$ and $\gamma_{\min}$ also scale with γ_0. Then the emissivity becomes

$$\epsilon(\nu)d\nu \propto \frac{d\gamma}{dt} \frac{n_T}{\gamma_0} f\left(\frac{\gamma}{\gamma_0}\right) d\gamma . \tag{1}$$

At a fixed B, any frequency is related to an energy, γ, by

$$\nu \propto \gamma^2 B ,$$

and

$$d\nu \propto \gamma B d\gamma . \tag{2}$$

We now examine the situation where the variables n_T, γ_0, and B are all functions of position, $\boldsymbol{r}$, in the source. Our observing frequency, $\nu_{\rm obs}$, corresponds to a $\gamma_{\rm obs}(\boldsymbol{r})$ such that

$$\nu_{\rm obs} \propto \gamma_{\rm obs}^2(\boldsymbol{r}) B(\boldsymbol{r}) . \tag{3}$$

And we assume, for simplicity, that γ_0 and B are uniform along the line of sight. Complications arising from line-of-sight inhomogeneities will be discussed in a later paper. The observed intensity

$$I(\nu_{\rm obs}, \boldsymbol{r}) \propto \epsilon(\nu_{\rm obs}, \boldsymbol{r}) L(\boldsymbol{r}) ,$$

where $L(\boldsymbol{r})$ is the path length through the source, and can be rewritten, using equations (1), (2), and (3) as

$$I(\nu_{\rm obs}, \boldsymbol{r}) \propto \sqrt{\nu_{\rm obs} B(\boldsymbol{r})}\, \frac{n_T(\boldsymbol{r})}{\gamma_0(\boldsymbol{r})} f\left[\frac{\gamma_{\rm obs}(\boldsymbol{r})}{\gamma_0(\boldsymbol{r})}\right] L(\boldsymbol{r}) , \tag{4}$$

where

$$\frac{\gamma_{\rm obs}(\boldsymbol{r})}{\gamma_0(\boldsymbol{r})} = \frac{1}{\gamma_0(\boldsymbol{r})} \sqrt{\frac{\nu_{\rm obs}}{B(\boldsymbol{r})}} . \tag{5}$$

Note that for the usual power-law distribution, and using equation (5),

$$f\left[\frac{\gamma_{\rm obs}(\boldsymbol{r})}{\gamma_0(\boldsymbol{r})}\right] \equiv \left(\frac{\gamma_{\rm obs}(\boldsymbol{r})}{\gamma_0(\boldsymbol{r})}\right)^{-x} \propto \left[\frac{1}{\gamma_0} \sqrt{\frac{\nu_{\rm obs}}{B}}\right]^{-x}$$

and

$$\begin{aligned} I(\nu_{\rm obs}, \boldsymbol{r}) &\propto \sqrt{\nu_{\rm obs} B(\boldsymbol{r})}\, \frac{n_T(\boldsymbol{r})}{\gamma_0(\boldsymbol{r})} L(\boldsymbol{r}) \nu_{\rm obs}^{-x/2} B^{x/2}(\boldsymbol{r}) \gamma_0^x(\boldsymbol{r}) \\ &\propto \nu_{\rm obs}^{(1-x)/2} B^{(1+x)/2}(\boldsymbol{r}) \end{aligned}$$

as expected (see, for example, Longair 1981).

Note that in the more general case of non-power-law distributions, the emissivity (eq. [4]) is a complicated function of n_T, B, and γ_0 because of the function $f[\gamma_{\rm obs}(\boldsymbol{r})/\gamma_0(\boldsymbol{r})]$. This means that observations at different frequencies $\nu_{\rm obs}$ may see very different brightness distributions on the sky.

In order to remove the frequency dependence from the observed intensity, we calculate the intensity not at some fixed $\nu_{\rm obs}$, but at a "reference" observing frequency, $\nu_{\rm ref}$, which varies with position in the source such that

$$\nu_{\rm ref}(\boldsymbol{r}) \propto \gamma_0^2(\boldsymbol{r}) B(\boldsymbol{r}) \tag{6}$$

Then, using equations (4) and (6),

$$\begin{aligned} I(\nu_{\rm ref}, \boldsymbol{r}) &\propto \sqrt{\nu_{\rm ref}(\boldsymbol{r}) B(\boldsymbol{r})}\, \frac{n_T(\boldsymbol{r})}{\gamma_0(\boldsymbol{r})} L(\boldsymbol{r}) f\left(\sqrt{\frac{\nu_{\rm ref}(\boldsymbol{r})}{B(\boldsymbol{r})}}\, \frac{1}{\gamma_0(\boldsymbol{r})}\right) \\ &\propto n_T(\boldsymbol{r}) B(\boldsymbol{r}) L(\boldsymbol{r}) , \end{aligned} \tag{7}$$

or

$$I(\nu_{\rm ref}, \boldsymbol{r}) \propto N_T(\boldsymbol{r}) B(\boldsymbol{r}) ,$$

where $N_T(\boldsymbol{r})$ is the total number of relativistic particles in the volume determined by the beam size and $L(\boldsymbol{r})$.

Equation (7) yields an important result. Note that by allowing the reference observing frequency to vary throughout the source, we have eliminated all the effects of the shape of the relativistic electron energy distribution, and constructed an intensity measure which is independent of observing frequency. We will call $I(\nu_{\rm ref}, \boldsymbol{r})$ the "corrected" intensity. Since the corrected intensity map has no dependence on $\gamma_0(\boldsymbol{r})$, it forms one of three maps which depend only on pairs of physical parameters as discussed further below.

2.2. *Construction of the Corrected Intensity Map*

In order to see how the corrected intensity map can be constructed, we consider the case of a simple parabolic shape to the logarithmic electron energy distribution (see Landau et al. 1986), which also yields a parabolic shape to the synchrotron spectrum

$$\ln[I(\nu_{\rm obs})] - \ln(I_{\max}) = -a[\ln(\nu_{\rm obs})]^2 .$$

This yields the following dependence of frequency-dependent spectral index $\alpha(\nu_{\rm obs})$ on the intensity

$$\begin{aligned} \alpha(\nu_{\rm obs}) = \left.\frac{d\ln[I(\nu)]}{d\ln(\nu)}\right|_{\nu_{\rm obs}} &= -2a \times \ln(\nu_{\rm obs}) \\ &= -\sqrt{4a \times \ln\left[\frac{I(\nu_{\rm obs})}{I_{\max}}\right]} . \end{aligned} \tag{8}$$

Since α is a directly measured quantity, we can then choose

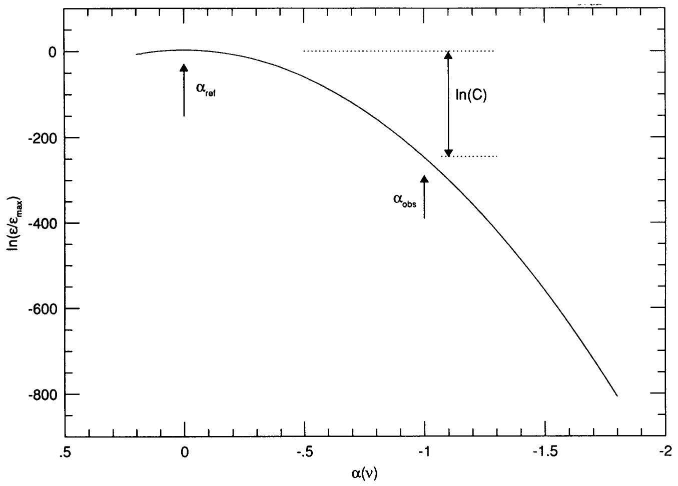

FIG. 1*a*

FIG. 1.—(*a*) The dependence of brightness on observed spectral index for a parabolic-shaped spectrum. The correction factor is based on the model brightness ratio between the observed spectral index and an arbitrary fiducial spectral index. (*b*) Illustration of the effects of the color-correction procedure. The spectra from two different positions in the source are displayed; one spectrum (solid line) has already been color-corrected. Shown for the uncorrected spectrum is an (arbitrary) observing frequency, which would yield an α_{obs} for each position and provide the input for the color-correction process. The correction can be thought of as a shifting of the spectrum in log frequency so that the α_{ref} of the uncorrected spectrum is at the same log (ν) as the previously corrected spectrum.

our reference observing frequency ν_{ref} by picking an arbitrary, fixed value of α, called "α_{ref}." All intensities will then be normalized to the value they would have at the frequency, ν_{ref}, where $\alpha(\nu_{ref}) = \alpha_{ref}$. At each position in the source, we then correct the intensity to the value it would have if observed at ν_{ref}. In our simple case, if we choose $\alpha_{ref} = 0$, we have

$$\ln(I[\alpha_{ref}]) = \ln(I[\alpha_{obs}]) + \ln(C) = \ln(I[\alpha_{obs}]) + \alpha_{obs}^2/4a\ , \quad (9)$$

where the correction factor, $\ln(C)$, is derived from equation (8), since $I = I_{max}$ at $\alpha_{ref} = 0$. This procedure is illustrated in Figure 1*a*.

As a final note on the effects of the color correction, consider the commonly used case of spectra consisting of a low-frequency power law, with a break at high frequencies. In this circumstance, the color-correction procedure is of limited value. As the observed spectral index approaches the low-frequency value, the correction factor becomes highly uncertain. In the low-frequency limit, when $\alpha(\nu) = \text{constant}$, no correction can be made.

2.3. *Constructing Maps of the Other Two Parameter Pairs*

Another way to visualize this color-correction procedure is to consider it as a translation along the log frequency axis. In other words, the correction is equivalent to picking a reference observing frequency and then sliding the spectrum in log frequency until $\alpha_{obs} = \alpha_{ref}$. This is illustrated in Figure 1*b*.

So, knowing the shape of the spectrum, we can use the spectral index map to construct a map of $\log[\Delta(\boldsymbol{r})]$, the amount the spectrum has shifted along the log frequency axis relative to some fiducial spectrum:

$$\log[\Delta(\boldsymbol{r})] = \log[\nu_{ref}(\boldsymbol{r})] - \log(\nu_{obs})$$

or

$$\Delta(\boldsymbol{r}) = \frac{\nu_{ref}(\boldsymbol{r})}{\nu_{obs}} \propto \gamma_0^2(\boldsymbol{r})B(\boldsymbol{r})\ .$$

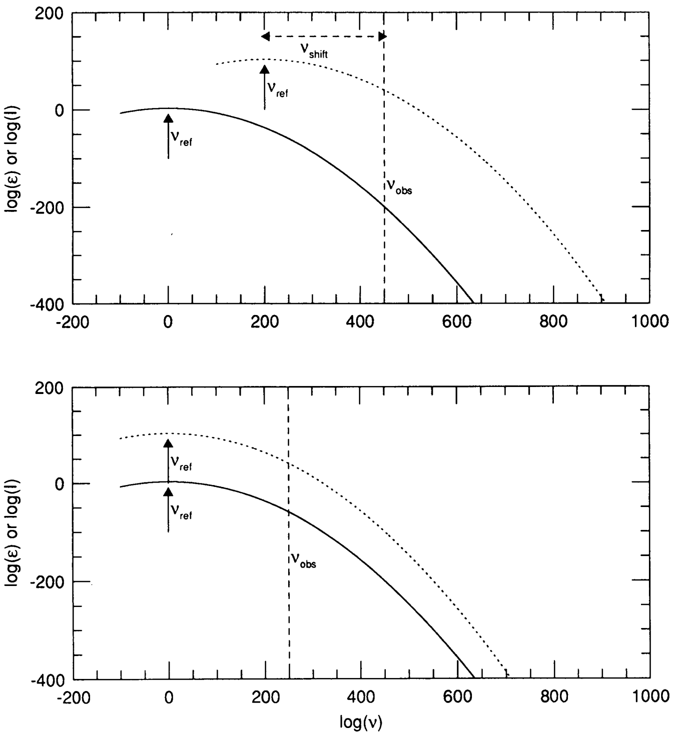

FIG. 1*b*

This is the second map of isolated parameter pairs. Note that we do not determine $\gamma_0^2(\boldsymbol{r})$ or $B(\boldsymbol{r})$ individually, but only the product $\gamma_0^2(\boldsymbol{r})B(\boldsymbol{r})$. The final isolated pair comes from dividing the first pair $[N_T(\boldsymbol{r})B(\boldsymbol{r})]$ by the second pair $[\gamma_0(\boldsymbol{r})^2 B(\boldsymbol{r})]$ yielding

$$\frac{N_T(\boldsymbol{r})}{\gamma_0^2(\boldsymbol{r})}\ .$$

3. DETERMINING THE RELATIVE IMPORTANCE OF B, N, AND γ

It may seem that we have derived all possible information from the original total intensity map and the spectral index map by constructing the three maps of paired parameters ($N_T B$, N_T/γ_0^2, and $\gamma_0^2 B$). But even qualitative comparison of these three maps can yield more insight by looking at the contrast between different positions on the maps.

Since each map is missing one of the three parameters, if a feature appears in two of the maps but not in the third, then the parameter that is absent in the third map is primarily responsible for the emissivity of that feature.

To illustrate these points, we have modeled a simple source. The model (Fig. 2[left] [Pl. 1]) includes (1) a single-valued magnetic field at every point where the value depends only on azimuthal angle; (2) a total relativistic electron density which is a sawtooth pattern in radius (four cycles) and azimuthally symmetric; and (3) a parabolic distribution (in the log) of electron energies, whose peak energy γ_0, is only a function of radius. Using the width of the Cygnus A spectrum to choose the parameters of our model energy parabola we have

$$f\left[\frac{\gamma}{\gamma_0(\boldsymbol{r})}\right] \propto e^{-1.4\{\log[\gamma/\gamma_0(\boldsymbol{r})] + 0.8\}^2}$$

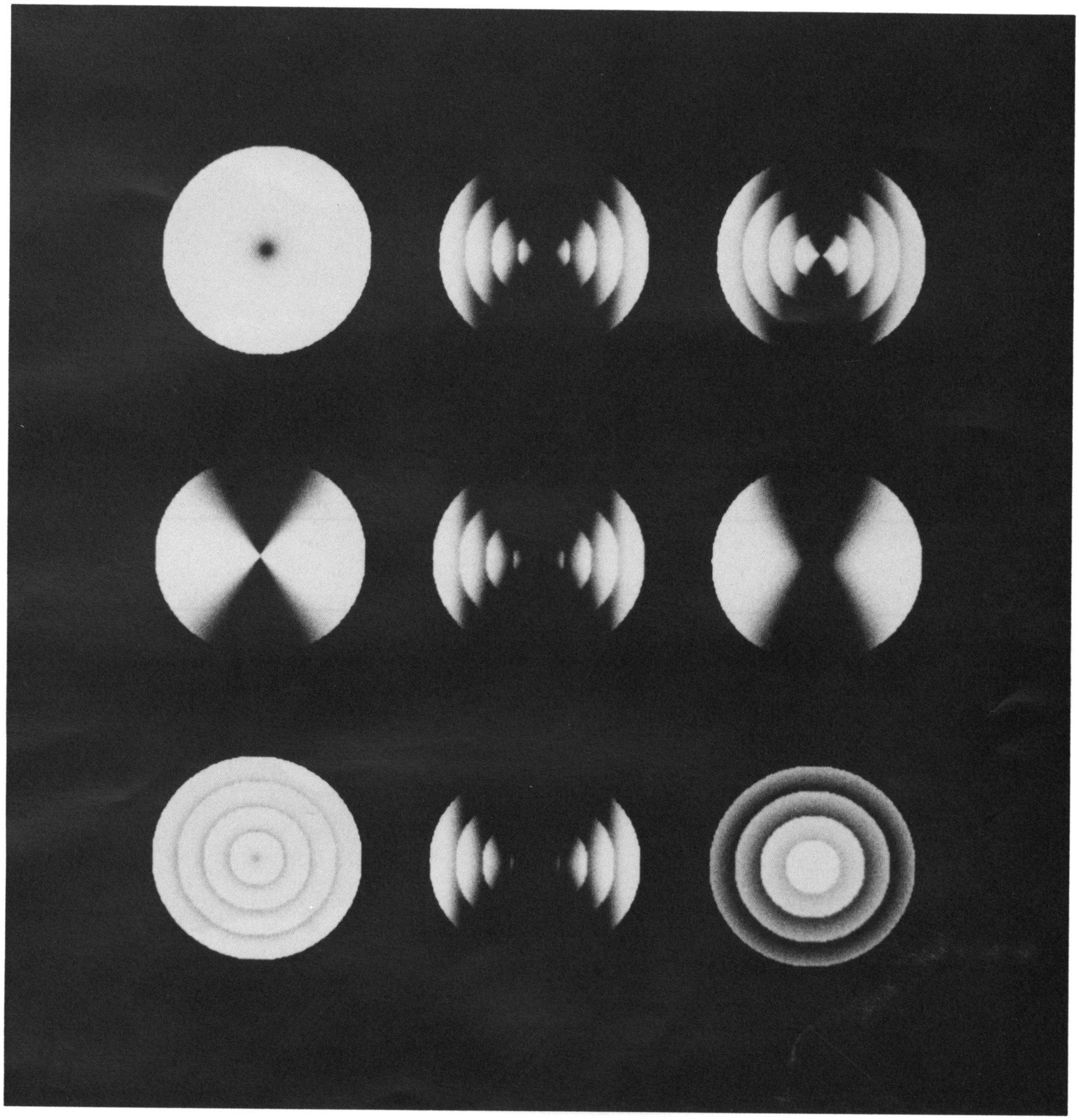

FIG. 2.—*Left:* This shows the input parameters of the model synchrotron source. The relativistic electron density (*bottom*) is a sawtooth function of radius. The magnetic field (*middle*) is only a function of azimuthal angle. The peak of the energy density distribution is only a function of radius (*top*). *Center:* These are what the model source would look like at three frequencies in the ratio 1 (*top*):30 (*middle*):100 (*bottom*). The source looks similar at the three frequencies. *Right:* These are the three parameter pairs. The top panel shows $N_T B$; the middle shows $\gamma_0^2 B$; and the bottom shows N_T/γ_0^2. In this simple model, it is easy to see that features disappear in each of the pair isolated maps. For example, in $\gamma_0^2 B$ there are no rings; the rings are due to variations in density.

KATE-STONE & RUDNICK (see ~~425~~, 118)
426

and

$$I(\nu_{\rm obs}, r) = \frac{\gamma}{\gamma_0(r)} B(r) N_T(r) e^{-1.4\{\log[\gamma/\gamma_0(r)]+0.8\}^2} .$$

We use this expression to show what the model would look like if we observed it at three frequencies in the ratios 1:30:100 (Fig. 2 [center]). Like a real source, the model shows only small variations between the three different frequencies, but none of them allow us to separate the B, N_T, or γ_0 dependencies.

In Figure 2(right), we show maps of the three parameter pairs ($N_T B$, N_T/γ_0^2, and $\gamma_0^2 B$). These three maps look quite different from one another. Let us consider a particular difference—both the $N_T B$ and the N_T/γ_0^2 maps show four concentric bands which do not appear in the $\gamma_0^2 B$ map. Using the method of looking for missing features in one of these maps, we would conclude that the rings are dominated by density differences as we know to be the case for this model (see Fig. 2 [left]).

The previous example illustrates the potential of separating N_T, γ_0 and B, but it oversimplifies the process. When a feature is noticeable, it is because one or more parameters are different

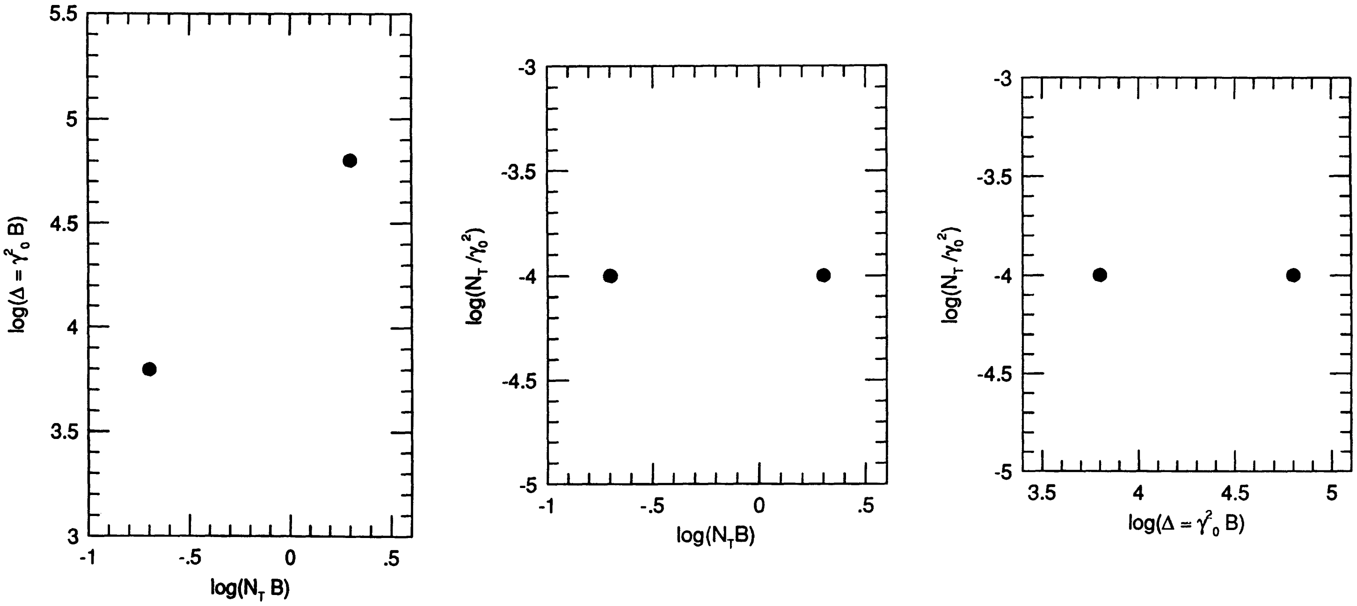

FIG. 3*a*

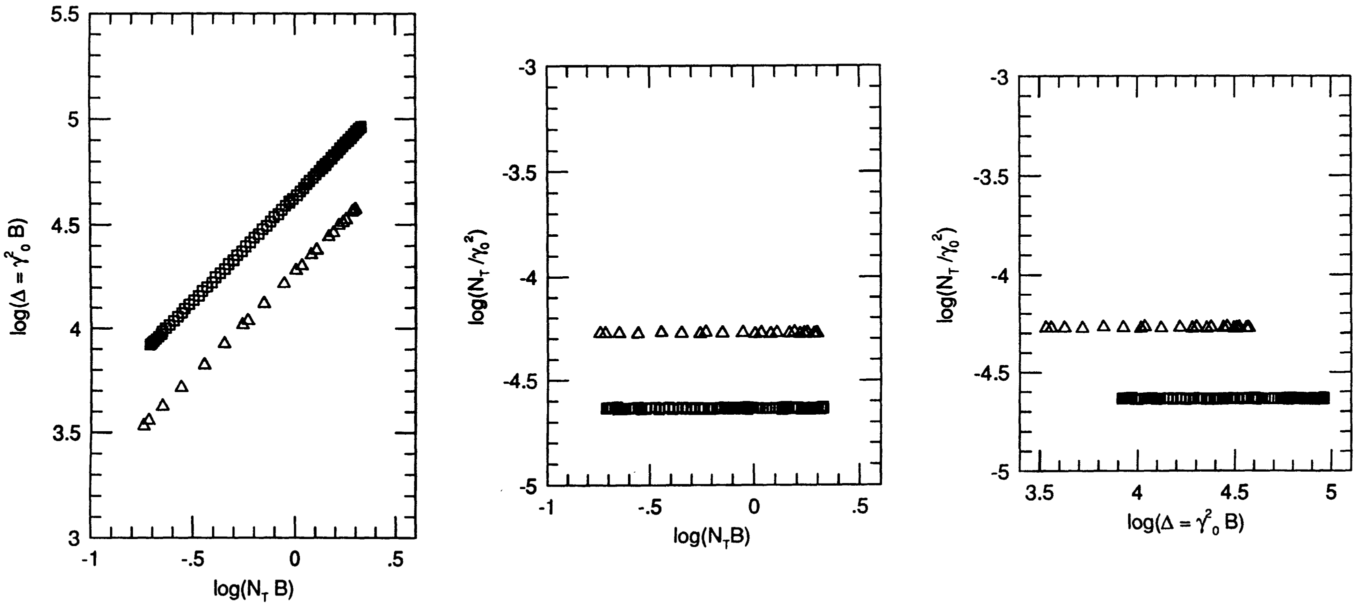

FIG. 3*b*

FIG. 3.—(*a*) Each parameter pair is plotted vs. the other two pairs. In this simple example, two positions in a fictitious source are shown; these points have the same $\log(N_T/\gamma_0^2)$ and lie along the slope of one on the plot of $\log(N_T B)$ vs. $\log(\gamma_0^2 B)$. Together these plots imply that the difference between these two positions is due to a difference in the magnetic field. (*b*) These plots are from two rings from the model source. The variation in emissivity in either ring is due to a variation in the magnetic field. The difference between the large ring and the small ring is due to differences in $\log(N_T/\gamma_0^2)$.

1994ApJ...426..116K

from those surrounding it. When only *one* parameter is different, it is possible to isolate it. Otherwise, the method of looking for missing features becomes very difficult.

We need a way to make these comparisons between the three parameter pairs quantitative and extend them to all points in the source, not just between adjacent places. We do this by plotting the log of each parameter pair versus the log of the other two parameter pairs for different positions in the source. Consider two positions in some source as shown in Figure 3*a*. These points have the same value of $\gamma_0^2 B$. The difference between these two points in log $(N_T B)$ equals the difference in log (N_T/γ_0^2). We would conclude that these two places have a different emissivity due to a difference in relativistic electron density. It is possible, though not plausible, that an increase in log (B) has been exactly compensated for by a decrease in log (γ_0^2). Thus, we can use these three plots to quantitatively compare any two positions in the source. However, if points appeared to be scattered randomly throughout the three diagrams, deconvolving the three parameters becomes very complicated, perhaps even impossible; this is the subject of a future paper.

In Figure 3*b*, we show the paired parameter plots for two concentric circular slices taken from our model. In both sets of plots, we see that log (N_T/γ_0^2) is a constant and log $(\gamma_0^2 B) \propto$ log $(N_T B)$. This implies that differences in emissivity about a circular slice are due to changes in the magnetic field as we know to be the case. Comparing the plots made from the larger circular slice to those made from the smaller one, we see that the slopes on the corresponding plots are the same, but that the intercepts differ. This would imply that the difference in emissivity between the two circles is due to a variation in N_T/γ_0^2 which may reflect a difference in N_T or γ_0^2 or both.

We have shown, using our simple model, how the construction of paired parameter maps, and plots between all pairs of maps for selected positions in the source, can lead to a successful deconvolution of the underlying physical parameters. By applying this technique to actual synchrotron sources, we may seek a new level of understanding of the structure and evolution of the relativistic plasma.

4. APPLICATION TO CYGNUS A

4.1. *Color Correction and the Resulting Maps*

We have applied the color-correction procedure to the VLA[1] maps of Cygnus A (Carilli et al. 1991), kindly supplied by C. Carilli. Both the 20 and 6 cm maps were corrected using the spectral index between these two frequencies, giving very similar results. The global spectral shape needed for the correction (the analogy of the parabola above) was determined using the color-color diagram introduced by KRA, and verified using the unique multifrequency data set available for Cygnus A. KRA found that several different mathematical approximations to the spectral shape were successful; here, we use a polynomial approximation determined using the 91, 20, and 6 cm data.

The 20 cm total intensity map and the spectral index map are shown in Figure 4*a* (Plate 2). The color-corrected map $(N_T B)$, the "color-correction" map $(\Delta = \gamma_0^2 B)$, and the N_T/γ_0^2 map are shown in Figure 4*b* (Plate 3).

In the $N_T B$ map, the hot spots and bright ridges no longer strongly dominate the brightness. In the eastern lobe, the color-corrected structure is dominated by an edge-brightened channel girdled by rings. These features are visible in the original, uncorrected maps but are lost against the bright regions near the eastern hot spots. In the following section, we describe the newly recognized channel in some more detail.

4.2. *The Channel*

Figure 5 is a schematic showing the brightened edges of the channel from the $N_T B$ map and the location of the counterjet from the $\gamma_0^2 B$ map. This counterjet was previously seen at higher resolution (Carilli 1989). The counterjet is seen projected against the channel but does not go down the channel center. The true three-dimensional relationship between these features is uncertain, though the simplest assumption would be that the counterjet is interior to the channel.

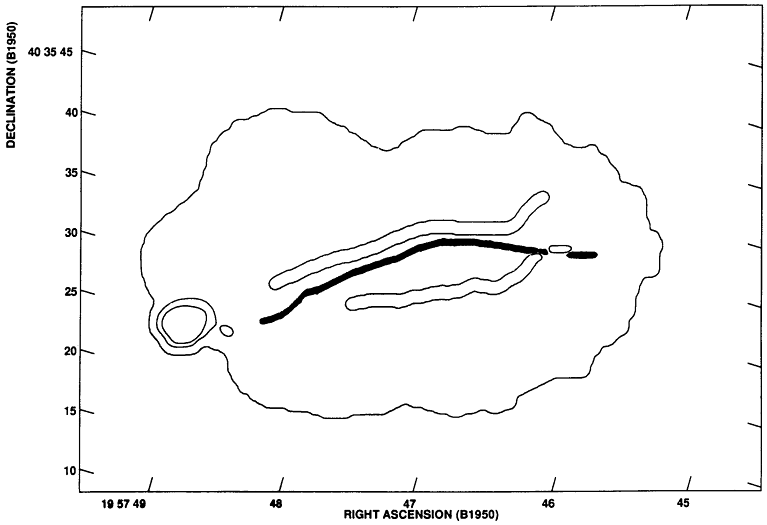

FIG. 5.—Schematic of features in the eastern lobe of Cygnus A. The long contours show the channel visible in a combination of locations from the corrected and original maps. The filled contour shows the counterjet, visible in patches along its length in the "correction map." The other contours show the location of the hot spots and outline the eastern lobe.

---

[1] The Very Large Array is a facility of the National Radio Astronomy Observatory, operated by Associated Universities, Inc., under contract with the National Science Foundation.

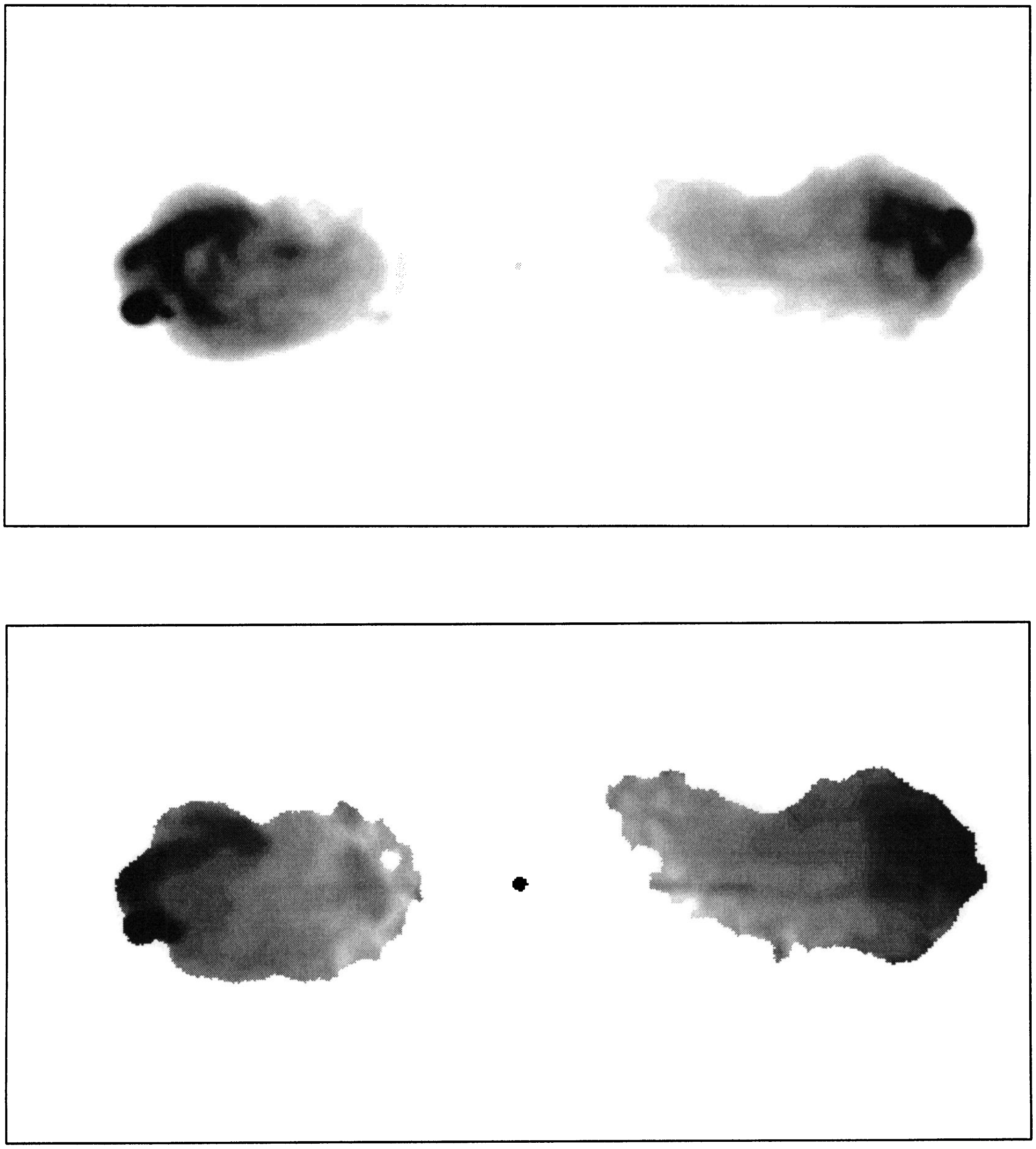

FIG. 4*a*.—Gray-scale image of Cygnus A at 1.4 GHz, from the data of Carilli et al. The beam size is $1''.5$. The top panel shows the original image. The bottom panel shows the map of spectral index (α).

KATE-STONE & RUDNICK (see ~~425~~, 120)
426

1994ApJ...426..116K

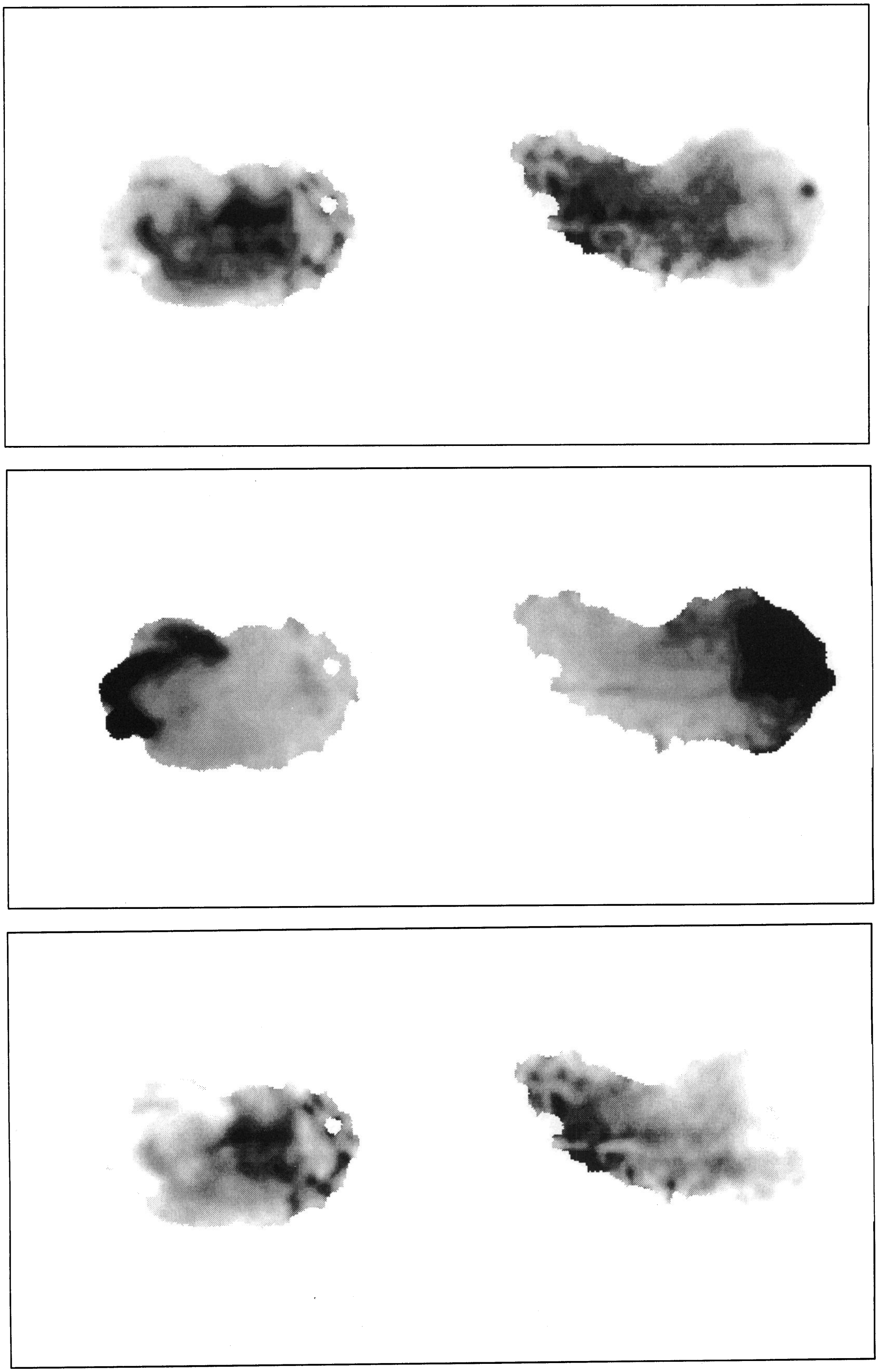

FIG. 4*b*.—More gray scale images of Cygnus A. The top panel shows the color-corrected map ($N_T B$). The middle map is the shift-in-frequency map ($\gamma_0^2 B$). The bottom map is the division of the two previous maps (N_T/γ_0^2).

KATE-STONE & RUDNICK (see ~~425~~, 120)
426

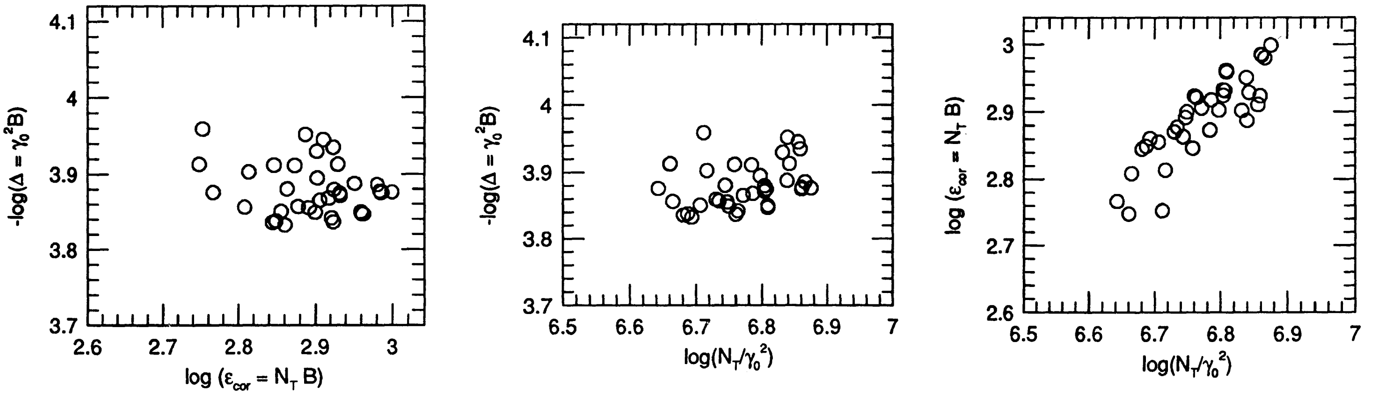

FIG. 6*a*

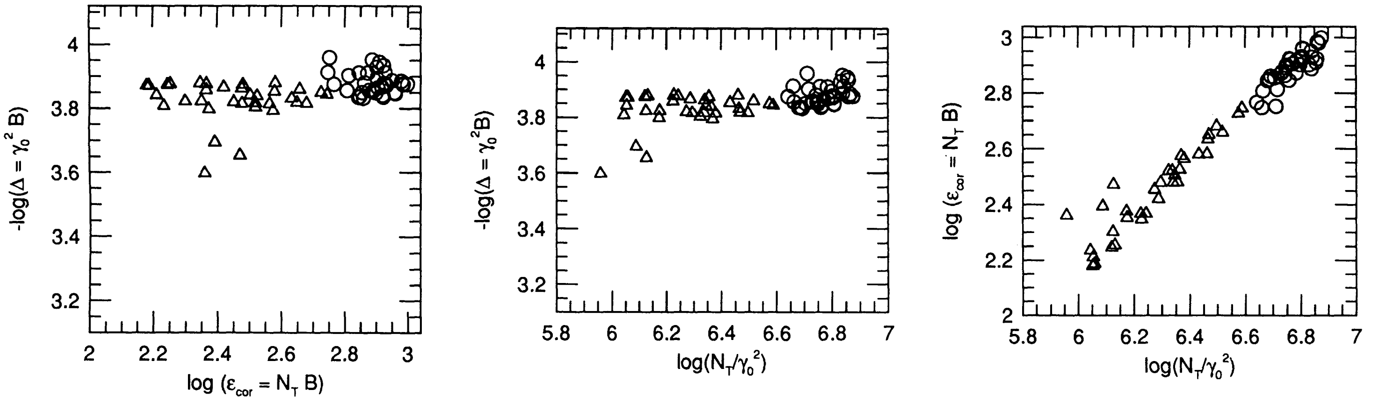

FIG. 6*b*

FIG. 6.—(*a*) The three parameter pairs are plotted here for a rectangular region all within the channel. Each point is independent. The first two plots on the left are consistent with a slope of zero and the third with a slope of 1. This implies that variations within the channel are due to variations in density. (*b*) The channel points (*circles*) from (*a*) are plotted along with points from a rectangular region north of the channel (*triangles*). The channel points lie along the same line as the other points, but in all three diagrams the channel points have a higher number of relativistic electrons than the local background lobe.

In Figure 6*a*, we show plots of the three parameter pairs against one another for each independent point within an $4''.5 \times 13''.0$ box around the brightest region of the channel. In both $\log (N_T B)$ versus $\log (\gamma_0^2 B)$ and $\log (N_T/\gamma_0^2)$ versus $\log (\gamma_0^2 B)$, the slope of the best-fit line is consistent with zero, and in $\log (N_T/\gamma_0^2)$ versus $\log (N_T B)$ the slope of the best-fit line is consistent with one. From this we see that $\log (\gamma_0^2 B)$ is constant throughout this area and variations in emissivity are due to variations in the number of electrons along the line of sight.

The channel is prominent in both the N_T/γ_0^2 and the $N_T B$ maps, but is not visible in the $\gamma_0^2 B$. This indicates that the appearance of the channel is due to the channel having a larger number of relativistic particles along the line of sight than neighbouring points in the lobe. If the path length through the lobe is at least the same as that through the channel, this represents a real relativistic particle density enhancement in the channel.

We can also see this density enhancement of the channel in the plots of the three parameter pairs against one another. In Figure 6*b*. we have plotted the same points from the channel as in Figure 6*a* as well as points from a rectangular region just north of the channel. From these plots, we can see that the channel has approximately the same value for $\log (\gamma_0^2 B)$ as the region to the north, but that the density of the channel is greater than the northern region. As a further note, the variations in the emissivity of this northern region (like the channel) are due to variations in density.

Features similar to the channel and rings have not been seen in any two-dimensional or three-dimensional hydrodynamic simulations, either with or without magnetic fields (e.g., Clark 1990). The lack of these features in the simulations and their apparent dependence on density alone probably implies a fundamental inadequacy in the physical conditions and/or processes built into the hydrodynamic simulations. It is hard to conceive of a process that changes the number of relativistic particles without changing the magnetic field or energy distribution of particles. The channel and rings remain a challenge to our understanding of the flows in extragalactic sources.

We wish to thank Chris Carilli for making his data on Cygnus A available and R. Perley, T. W. Jones, T. J. Jones, J. Dickey, and the referee, Geoffrey Bicknell, for helpful discussions and comments. This study was supported in part by the National Science Foundation grant AST 91-00486 to the University of Minnesota.

REFERENCES

Bicknell, G. V. 1986, ApJ, 300, 591

Carilli, C. L., Dreher, J. W., & Perley, R. A. 1988, in Hot Spots in Extragalactic Radio Sources, ed. K. A. Meisenheimer & H.-J. Roser (Berlin: Springer-Verlag), 51

Carilli, C. L., Perley, R. A., Dreher, J. W., & Leahy, J. P. 1991, ApJ, 383, 544

Clarke, D. A. 1990, in IAU Symp. 140, Galactic and Intergalactic Magnetic Fields, ed. R. Beck, P. P. Kronberg, & R. Wielebinski (Dordrecht: Kluwer), 412

Katz-Stone, D., Rudnick, L., & Anderson, M. C. 1993, ApJ, 407, 549

Landau, R., et al. 1986, ApJ, 308, 78

Longair, M. S. 1981, High Energy Astrophysics (Cambridge: Cambridge Univ. Press)

Miley, G. K. 1976, In Proc. Nato Summer School, Physics of Nonthermal Radio Sources, ed. G. Setti (Dordrecht: Reidel), 1

Meisenheimer, K. A., Roser, H.-J., Hiltner, P. R., Yates, M. G., Longair, M. S., Chin, R., & Perley, R. A. 1989, A&A, 219, 63

Norman, M. L., Smarr, L., Winkler, K.-L. A., & Smith, M. D. 1982, A&A, 113, 285

van Breugel, W., Miley, G., Heckman, T., Butcher, H., & Bridle, A. 1985, ApJ, 290, 496